applied sciences

MDPI

Article

Electromagnetic Interference Shielding Analysis of Hybrid Buckypaper-Reinforced Polymer Matrix Composites: A Quantum Tunneling-Informed Equivalent Circuit Approach

Kartik Tripathi [1], Mohamed H. Hamza [1], Madeline A. Morales [2], Todd C. Henry [2], Asha Hall [2] and Aditi Chattopadhyay [1,*]

[1] School for Engineering of Matter, Transport and Energy, Arizona State University, Tempe, AZ 85287, USA; ktripat3@asu.edu (K.T.); mhamza1@asu.edu (M.H.H.)
[2] DEVCOM Army Research Laboratory, Aberdeen Proving Ground, Aberdeen, MD 21005, USA; madeline.a.morales.civ@army.mil (M.A.M.); todd.c.henry2.civ@army.mil (T.C.H.); asha.j.hall.civ@army.mil (A.H.)
* Correspondence: aditi@asu.edu

Abstract: A novel modeling approach is developed for investigating the effectiveness of buckypaper (BP), a porous membrane made of a highly cross-linked network of carbon nanotubes, in improving the electromagnetic interference (EMI) shielding properties of carbon fiber-reinforced polymer (CFRP) composites. The methodology uses quantum tunneling-based equivalent electrical circuits and Monte Carlo simulations to predict the frequency-dependent electrical conductivity and EMI shielding effectiveness (SE) of the hybrid BP/CFRP composites. The study examines a signal frequency range of 50 MHz to 12 GHz that includes the very high and X-band. The results show that at a frequency of 12 GHz, the transverse conductivity increases to approximately 12.67 S/m, while the longitudinal conductivity decreases to about 3300 S/m from an initial value of 40,000 S/m. These results are then integrated into the ANSYS High-Frequency Structure Simulator to predict SE by simulating the propagation of electromagnetic waves through a semi-infinite composite shield element. The numerical simulations illustrate that incorporating BP significantly improves the SE of CFRP composites beyond 2 GHz owing to its high conductivity in that frequency range. For instance, at 12 GHz signal frequency, adding a single BP interleaf enhances the SE of a [90, 0] laminate by up to ~64%.

Keywords: carbon nanotubes; buckypaper; EMI shielding; electrical conductivity; quantum tunneling; CFRPs; polymer composites

Citation: Tripathi, K.; Hamza, M.H.; Morales, M.A.; Henry, T.C.; Hall, A.; Chattopadhyay, A. Electromagnetic Interference Shielding Analysis of Hybrid Buckypaper-Reinforced Polymer Matrix Composites: A Quantum Tunneling-Informed Equivalent Circuit Approach. *Appl. Sci.* **2024**, *14*, 8960. https://doi.org/10.3390/app14198960

Academic Editor: Mario Lucido

Received: 9 September 2024
Revised: 1 October 2024
Accepted: 2 October 2024
Published: 4 October 2024

1. Introduction

The increased use of electronics in aerospace structures and other applications underscores the need to develop effective electromagnetic interference (EMI) shielding strategies for protecting sensitive electronic systems from external electromagnetic signals. Carbon nanotubes (CNTs) have emerged as a promising material due to their remarkable properties, such as high tensile strength (100 GPa) and stiffness (1 TPa), excellent thermal conductivity (~3500 W/m/K) and electrical conductivity (~105 S/m) and have many potential applications in aerospace such as de-icing and lightning strike protection [1,2].

For EMI shielding applications at the structural scale, harnessing the full potential of CNTs poses a substantial challenge [3]. Researchers have explored the utilization of CNT-doped resins as a matrix in composite material systems to attain desired electrical properties [4–9]. Du et al. [5] utilized a coagulation technique to fabricate a nanocomposite consisting of single-walled carbon nanotubes (SWCNT) and polymethyl methacrylate (PMMA), achieving an electrical conductivity of 10^{-3} S/m with a 2% SWCNT weight fraction. Sawi et al. [6] extensively investigated the electrical conductivity of double-walled carbon nanotubes within an epoxy-based RTM6 matrix, analyzing its frequency and

temperature dependence. Although the doping approach enhances overall properties, it is limited in harnessing the full potential of CNTs due to challenges in incorporating high CNT weight fractions. Primarily, CNTs tend to agglomerate due to van der Waals forces, resulting in property variations at larger scales [10–14].

Additionally, high CNT weight fractions elevate resin viscosity, impeding resin flow during fabrication. Porous membranes composed of interconnected CNTs, known as buckypaper (BP), offer a viable solution by enabling the incorporation of high weight fractions of CNTs and ensuring their uniform dispersion throughout the composite structure [15]. These films facilitate strong interlaminar bonds, making them compatible for integration into laminate structures, hence this approach overcomes the issues associated with CNT-doped resin in composite applications [16]. Due to its high electrical conductivity, homogenous dispersion through the resin microstructure, and carbon fiber reinforced polymer (CFRP) stiffness and strength enhancement [17], BP is selected as a promising candidate to investigate its EMI shielding performance within various CFRP laminate configurations.

The most common EMI shielding strategy involves utilizing conductive barriers to block unwanted external electromagnetic signals that might disrupt the internal circuitry. CFRP composites, which are increasingly being used in aerospace applications, are capable of EMI shielding due to the presence of electrically conductive fibers [18]. However, unidirectional CFRP composites exhibit significant anisotropy in electrical conductivity, attributed to the distinct mechanisms manifesting in the longitudinal and transverse directions. Along the fiber direction, the electrical conductivity of the lamina closely aligns with that of the fibers, whereas in the transverse direction, obtaining consistent conductivity values is challenging.

In contrast to longitudinal conductivity, transverse conductivity exhibits significant variability and unpredictability, which is primarily attributed to the stochastic arrangement of fibers and the variability in fiber volume fraction. The existing literature demonstrates a notable lack of consensus, as diverse studies offer dissimilar predictions for transverse conductivity values ranging from 10^{-5} to 30 S/m [8,9,19–22]. Banerjee et al. [19] used a tunneling model based on thermal activation energy and reported a transverse conductivity of ~0.04 S/m. Wasselynck et al. [20,21] used a theoretical model of impedance analysis with Monte-Carlo simulations to account for microstructure variability and predicted transverse conductivity to be approximately ~8 S/m. Accounting for the variability in microstructure and quantum tunneling phenomena is crucial for the accurate prediction of transverse conductivity [23]. When estimating the EMI shielding effectiveness (SE) at high frequencies (>1 GHz), relying on DC conductivity leads to inaccuracies due to the significant rise of the skin effect in an AC field as a result of induced eddy currents [24]. This phenomenon limits the flow of current to the outer surface of the conductor rather than a uniform distribution across the cross-section. Hence, an accurate prediction of the EMI shielding effectiveness of composites across a broad frequency spectrum is achievable solely through AC conductivity, and very limited work is reported in this area. Mohan et al. [8] employed a micromechanics model to predict the electrical conductivity in CNT-doped epoxy composites, showing a direct correlation between transverse electrical conductivity and frequency. The lack of a comprehensive model for predicting AC conductivity necessitates the need for a more accurate modeling approach that accounts for both microstructure variability and frequency dependence.

Various techniques have been investigated to enhance the EMI shielding performance of composite structures. Some researchers have used metallic layers or conductive coatings to enhance the reflective component of EMI shielding [24–26]. As observed in a previous study by the co-authors [24], the incorporation of copper mesh improves the reflection component of EMI shielding effectiveness. Yazdi et al. [25] have characterized the EMI shielding effectiveness of glass fiber reinforced polymer composites coated with aluminum, aluminum bronze and zinc. Their investigations show an enhanced SE of up to 60 dB from the baseline value of 7 dB. The major drawback associated with including metallic layers is that the structural strength is compromised due to its poor bonding with the composite ply.

The use of a modified epoxy with magnetic or conductive filler materials such as CNTs has been investigated [27,28]. Liu et al. [27] studied the EMI SE of nanocomposites by varying the weight fractions of different filler materials, including multi-walled carbon nanotubes (MWCNTs), Fe_3O_4, and Fe within the epoxy resin. Their work reported an upward trend of shielding effectiveness with increasing frequency by using CNTs, while the Fe and Fe_3O_4-doped composites showed a less frequency dependence. Zhang et al. [29] explored strategies for assembling two-dimensional metal carbide sheets (MXenes) to improve electromagnetic interference (EMI) shielding. They found that rGO/CoNi nanosheets exhibited a high absorption shielding effectiveness, achieving a value of 54.1 dB. Although these methods can be beneficial in enhancing both the electrical and mechanical properties of composites, they do not harness the full potential of carbon nanotubes at the laminate level [10–14]. This paper presents a novel approach for modeling the AC conductivity of BP-reinforced CFRP laminates accounting for quantum tunneling and skin effects.

The paper is structured into two main sections: the first section introduces an equivalent circuit method for characterizing the frequency-dependent electrical conductivity of carbon fiber lamina. The CFRP microstructure is transformed into an equivalent circuit, and the effective impedance is analyzed to estimate the longitudinal conductivity. The transverse conductivity is determined using Monte Carlo simulations informed by quantum tunneling principles. The second section focuses on coupling the estimated conductivity values with electromagnetic wave propagation simulations to investigate the EMI SE of hybrid BP/CFRP samples. Finally, the EMI SE results are compared with an alternative shielding technique using copper mesh layers.

2. Materials and Methods

To assess the AC conductivity, each CFRP lamina is modeled using polyacrylonitrile-based unidirectional IM7 carbon fiber and EPON-862 epoxy system comprising diglycidyl ether of bisphenol F (DGEBF) resin and diethylenetriamine (DETA) hardener. In the case of hybrid samples, Miralon S-T01AVB-12 sheets provided by Nanocomp Technologies (Merrimack, NH, USA) were employed as BP interleaves between the CFRP plies. A schematic of the hybrid composite and the BP morphology is shown in Figure 1 [17]. Relevant properties of fiber, resin, and BP are summarized in Table 1 [30–33]. For constructing the transverse representative volume element and establishing the equivalent circuit model, various parameters outlined in Table 2 were used. Table 3 contains some physical constants used in this study.

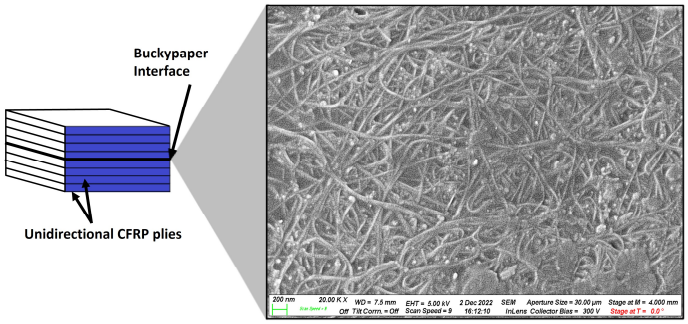

Figure 1. Hybrid laminate schematic showing BP microstructure obtained through SEM [17].

Table 1. Constituent electrical properties [30–33].

	DC Resistivity ρ_{DC} (Ω-m)	Relative Permittivity ε_r	Refractive Index n	Relative Permeability μ_r
Fiber	Longitudinal: 1.5×10^{-5} Transverse: 9.3×10^{-5}	1	1.6	1
Epoxy	10^8	3	1.55	1
BP	1.3×10^{-5}	1	-	1

Table 2. Relevant composite sample parameters used in the study.

Parameter (Unit)	Value
Fiber mean diameter (μm)	5.24
Fiber diameter standard deviation (μm)	0.295
Fiber volume fraction	0.6
CFRP lamina thickness (mm)	0.25
BP thickness (mm)	0.1

Table 3. Physical constants used in this study.

Parameter (Unit)	Value
Electron charge (C)	1.6×10^{-19}
Electron mass (kg)	9.11×10^{-31}
Permittivity of free space (F/m)	8.854×10^{-12}
Permeability of free space (H/m)	$4\pi \times 10^{-7}$
Reduced Planck's Constant (Js)	1.05×10^{-34}
Speed of light (m/s)	3×10^{8}

2.1. Electrical Conductivity Characterization of CFRPs

To characterize the frequency-dependent electrical conductivity of individual CFRP plies, longitudinal and transverse CFRP representative volume elements (RVE) are transformed into an equivalent electrical circuit consisting of inductors, capacitors, and resistors. Next, the impedance is analyzed, which is subsequently converted into complex conductivity based on the RVE dimensions.

2.1.1. Longitudinal Conductivity

For the longitudinal case, the analysis is based on the premise that in addition to their internal electrical resistance, the fibers also possess inductive effects, while the matrix acts as an insulating material. Figure 2 presents a graphical depiction of a unidirectional (UD) CFRP lamina, showcasing its microstructure and the associated equivalent circuit for the longitudinal orientation. As depicted, individual fibers are represented as a combination of a resistor (R) and an inductor (L) arranged in series. For the N parallel fibers, the overall circuit consists of N parallel resistor-inductor elements.

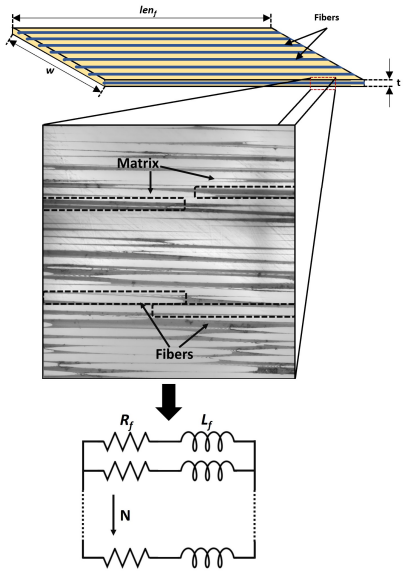

Figure 2. Microstructure of a unidirectional CFRP lamina and its equivalent electrical circuit in the longitudinal direction consisting of the N fibers, each having their own resistance (R_f) and inductance (L_f).

The resistance of each wire R_f can be expressed in terms of fiber resistivity ρ_f, length len_f, and radius r_f as follows:

$$R_f = \frac{\rho_f len_f}{\pi r_f^2} \tag{1}$$

The inductance of each fiber, denoted L_f, is expressed as a sum of its self-inductance and the mutual inductance of the neighboring fibers. The self inductance represented as $\left(L_f\right)_S$ can be expressed in terms of the fiber dimensions and vacuum permeability μ_o [34]:

$$\left(L_f\right)_S = \frac{\mu_o len_f}{2\pi} log\left(\frac{2len_f}{r_f} - 1\right) \tag{2}$$

For mutual inductance estimation, drawing upon the principles of Faraday's law of electromagnetic induction and Lenz's law when an alternating current flows through two parallel wires separated by a distance d, a counteracting current is induced. This happens because the changing current gives rise to a changing magnetic field through the surrounding wires. Consequently, a current is generated that resists this magnetic field change. This phenomenon within the CFRP microstructure is depicted in Figure 3a. The direction of the magnetic field can be determined using the right-hand rule, and its magnitude can be expressed as below:

$$B = \frac{\mu_o I}{2\pi d} \tag{3}$$

where I is the electric current traversing the fiber and d denotes the radial distance from the fiber to the point of interest. Figure 3b depicts magnetic field vectors within a small region of the ply cross-section and illustrates the influence of surrounding fibers on the magnetic field intensity at any given fiber location. For illustration, the fibers are color-coded to correspond with their respective magnetic field vectors, with an 'X' symbol denoting the direction of current flow into the plane. It should be noted that the effective magnetic field at the arbitrary fiber experiences significant cancellation due to the influence of surrounding fibers. However, it remains nonzero owing to the nonuniform distribution of fibers within the microstructure. Finally, using the relation between magnetic flux φ and wire inductance L, the final form of mutual inductance denoted by $\left(L_f\right)_M$ can be expressed as follows:

$$\left(L_f\right)_M = \frac{\varphi}{I} = \frac{B.A}{I} = \frac{2Blen_f r_f}{I} \tag{4}$$

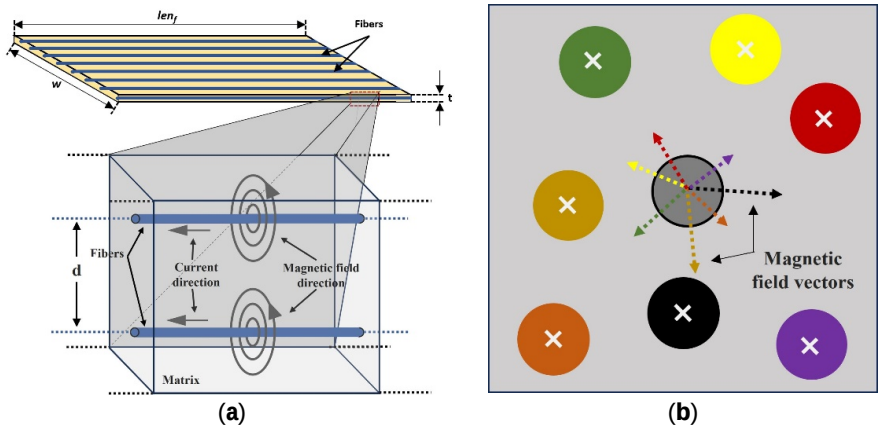

Figure 3. (**a**) Magnetic fields due to parallel fibers separated by a distance d and (**b**) color-coded magnetic field vectors due to the current carrying neighboring fibers.

Utilizing a transverse CFRP RVE as depicted in Figure 4a, assuming that the fibers are connected in parallel, the inductance for each fiber and ultimately the overall inductance $\left(L_f\right)_{net}$ was estimated by summing $\left(L_f\right)_M$ and $\left(L_f\right)_S$.

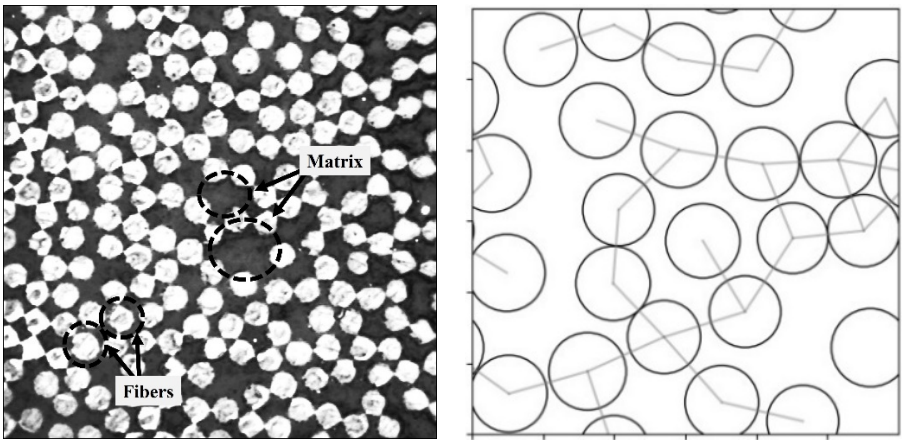

Figure 4. (**a**) Transverse microstructure showing the fiber distribution used for estimating the overall inductance, (**b**) Interconnected RVE with straight line connections between pairs of fibers within the threshold distance.

The magnitude of total impedance in the longitudinal direction can be expressed in terms of fiber resistance R_f, total inductive reactance X_L, and the number of fibers N using the relation given below:

$$\left|Z_{long.}\right| = \sqrt{\left(\frac{R}{N}\right)^2 + X_L^2} \tag{5}$$

where X_L is further expressed in terms of the total inductance $\left(L_f\right)_{net}$ and signal frequency f as follows:

$$X_L = 2\pi f\left(L_f\right)_{net} \tag{6}$$

Finally, the AC conductivity in the longitudinal direction σ_L can be expressed using the following equation:

$$\sigma_L = \frac{len_f}{A\left|Z_{long.}\right|} \tag{7}$$

where A is the cross-sectional area of the CFRP lamina perpendicular to the fiber direction.

2.1.2. Transverse Conductivity

In the context of transverse conductivity, two primary mechanisms come into play. First, during the fabrication process, the likelihood of fiber-to-fiber contact can give rise to a conductive pathway within the sample. Second, when the gap between two fibers is within a threshold distance, quantum tunneling through the highly resistant epoxy barrier becomes a possibility. This section presents an in-depth explanation of a probabilistic conductivity model that encompasses both of these phenomena in conjunction with Monte Carlo simulations.

Figure 4a illustrates the transverse microstructure of a CFRP lamina. Based on the morphology, a maximum fiber–fiber separation of 100 nm was selected for generating the RVE. A square RVE with 23 fibers was generated, accounting for the mean and standard deviation of fiber radius, range of fiber spacing, and fiber volume fraction. For a 60% fiber volume fraction, the resulting RVE size was ~28.75 μm. To gain insights into the spatial relationships between fibers and potential conductive pathways, a connectivity matrix

based on a threshold fiber pair distance (T) was established. It was observed that the tunneling probability was insignificant for fiber—fiber separation greater than 50 nm and was therefore chosen as the threshold for this study. This assumption is verified by the results presented in Section 3.2. Figure 4b illustrates the resulting connected RVE with doubly periodic boundaries, wherein all fiber pairs deemed potentially conductive are linked by straight lines.

Next, the connected RVE is analyzed to identify the shortest conductive pathway across the RVE. This pathway holds significance since electrical charges follow the route of least resistance. Subsequently, this shortest conductive path is subjected to a more in-depth analysis using principles of quantum tunneling to compute the transverse conductivity. The details of this methodology are presented in Figure 5. Finally, the Monte Carlo method was employed, which involved conducting 1000 simulations of the process outlined in Figure 5. The results were used to calculate the mean transverse conductivity.

To quantify the tunneling probability between each fiber pair within the conductive path, the one-dimensional, time-independent Schrödinger equation was solved, as given by Equation (8).

$$-\frac{\hbar^2}{2m_e}\frac{\partial^2\Psi(x)}{\partial x^2} + U(x)\Psi(x) = E\Psi(x) \tag{8}$$

where $\hbar$ is the reduced Planck's constant, m_e is the mass of the electron, and $\Psi(x)$ denotes the wave function of the particle at a given location x. The terms U and E represent the barrier potential energy and the particle energy, respectively. A schematic of fiber pairs with an enlarged view of the contact region is displayed in Figure 6. As illustrated in the figure, the fiber–fiber contact is divided into three regions. Regions A and C represent the fiber space, and region B represents the insulating matrix. By solving Equation (8) for each region individually, the unique wave functions Ψ_A, Ψ_B, and Ψ_C were computed.

The solutions to these wave functions, along with the derivation of the tunneling probability, is detailed in Appendix A. The final expression for the tunneling coefficient C_T is expressed as follows:

$$C_T = \left(1 + \frac{\sinh^2(k_b a)}{4\eta(1-\eta)}\right)^{-1} \tag{9}$$

where η represents the ratio of the particle's energy (E) to the barrier potential energy (U) and k_b is a constant. Equation (9) reveals that the likelihood of tunneling is directly proportional to the energy of the electrons and inversely proportional to the barrier size a. The potential energy of the barrier is estimated by an equivalent circuit approach. As depicted in Figure 7a, the contact impedance can be translated into an equivalent circuit comprising a resistor-capacitor parallel circuit pair. The magnitude of this impedance $|Z_c|$ is expressed below:

$$|Z_c| = \frac{1}{\sqrt{\frac{1}{R_c^2} + \frac{1}{X_c^2}}} \tag{10}$$

where R_c and X_c are the resistance and capacitive reactance of the matrix region at the contact. For a curved matrix geometry, as illustrated in Figure 7b, the contact resistance and capacitive reactance is estimated by discretizing the matrix region and integrating. Their simplified expressions are as follows:

$$R_c = \frac{\rho_m}{len_f I} \tag{11}$$

$$X_c = \frac{1}{2\pi f C_c} \tag{12}$$

The contact capacitance C_c can be further expressed in terms of the material's relative permittivity ε_r and permittivity of free space ε_o as follows:

$$C_c = \varepsilon_o \varepsilon_r l_c I \tag{13}$$

The term l_c denotes the fiber contact length, which is defined as the total length of the segment along the fiber direction where fibers consistently remain in close proximity. It's important to distinguish this term from the sample length along the fiber direction, as fibers exhibit a wavy, nonlinear nature, as illustrated in Figure 8. l_c was chosen as a percentage of the overall RVE length for which the wavy fibers maintain proximity. In Equations (11) and (13), the term I is a constant and can be expressed as shown below:

$$I = \int_0^{\frac{\pi}{2}} \frac{\cos\theta d\theta}{\left(\frac{T}{2r_f} - \cos\theta\right)} \tag{14}$$

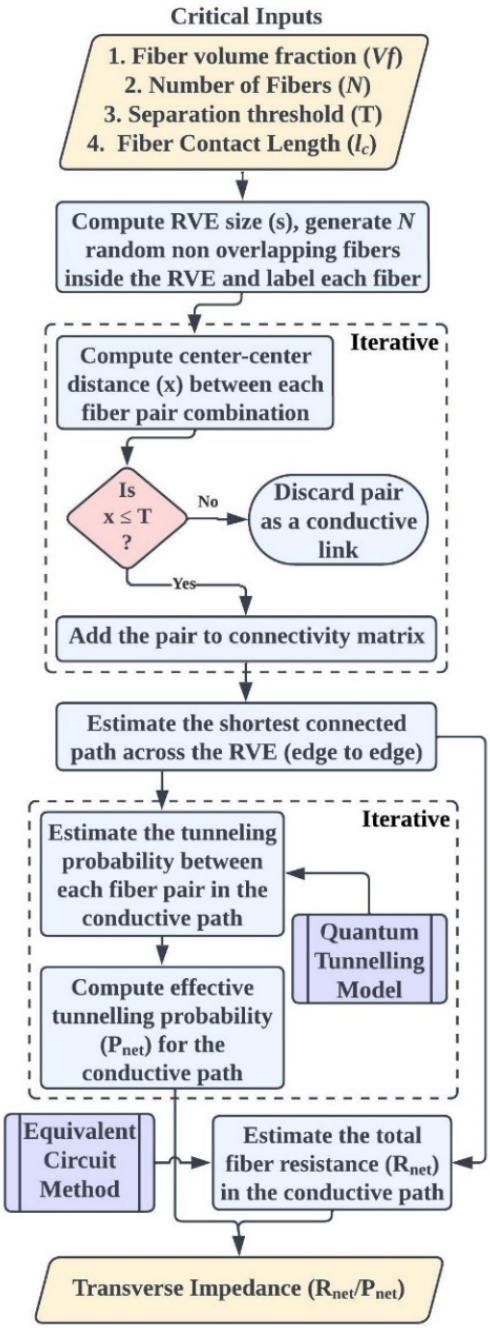

Figure 5. Transverse conductivity model outline.

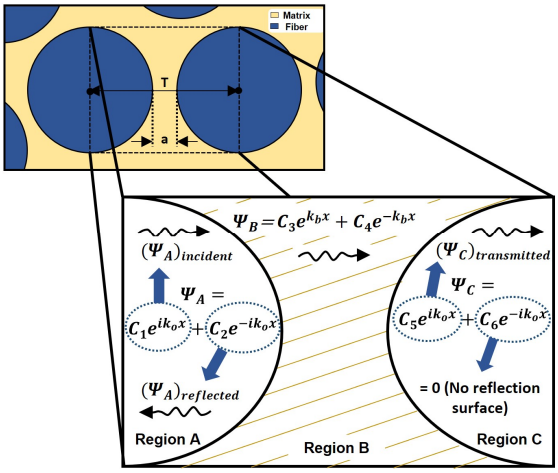

Figure 6. Fiber pair schematic with an enlarged view of the contact region showing the wave functions (Ψ) for different regions along the particle tunneling path.

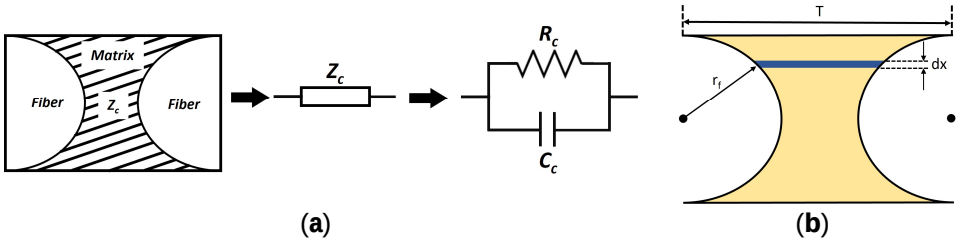

Figure 7. (**a**) Equivalent circuit of a fiber–fiber contact pair and its equivalent contact impedance (Z_c) and (**b**) contact region discretization for determining effective contact resistance (R_c) and capacitance (C_c).

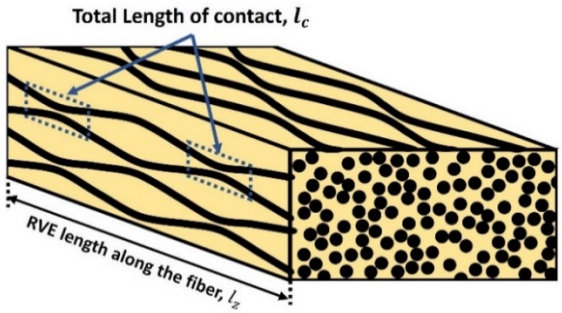

Figure 8. Schematic showing the fiber contact length (l_c) due to fiber waviness.

The energy required to transmit an electron through the matrix barrier is calculated from the energy, current, and voltage relationship as follows:

$$U = I_{rms}^2 \left| Z_c \right| \Delta t \tag{15}$$

where I_{rms} is the RMS current of the signal, and Δt is the time taken by the particle to pass through the barrier. Upon simplifying Equation (15) further, we obtain the following expression for the barrier potential energy U:

$$U = \frac{{q_e}^2 c \left| Z_c \right|}{a n_m} \tag{16}$$

where q_e, c, and n_m are the electron charge, speed of light, and refractive index of the matrix, respectively. The term c/n_m denotes the speed of electrons in the matrix medium. The energy of the particle E is expressed as follows:

$$E = 2\pi\hbar f \tag{17}$$

The shortest conductive path is analyzed next to determine the effective transverse impedance. Using Equation (9), the specific tunneling probabilities $(P_{link})_n$ associated with each n^{th} fiber–fiber link within the conductive path can be calculated. Figure 9 visually represents the electron tunneling process along the shortest route. The cumulative tunneling probability across the RVE, denoted as P_{net}, can be expressed as the product of individual tunneling probabilities for all links as shown below:

$$P_{net} = \prod_{n=1}^{N_l} (P_{link})_n \tag{18}$$

where N_l corresponds to the total number of fiber–fiber links in the conductive path. In a hypothetical scenario where all the fibers along the conductive path are touching ($P_{net} = 1$), the overall RVE impedance can be determined by summing the resistance across each fiber cross-section within the conductive path. This cumulative impedance, denoted as R_{net}, can be mathematically represented as follows:

$$R_{net} = \sum_{n=1}^{N_f} \left(R_{ft}\right)_n \tag{19}$$

where N_f denotes the total number of fibers in the conductive path and $\left(R_{ft}\right)_n$ is the resistance across the n^{th} fiber cross-section. Here, the subscript ft refers to the transverse fiber resistance. Finally, the RVE impedance $|Z_c|_{RVE}$ and transverse conductivity σ_T are determined by the following relations:

$$|Z_c|_{RVE} = \frac{R_{net}}{P_{net}} \tag{20}$$

$$\sigma_T = \frac{1}{l_z |Z_c|_{RVE}} \tag{21}$$

where l_Z is the length of the RVE along the fiber direction, as labeled in Figure 8.

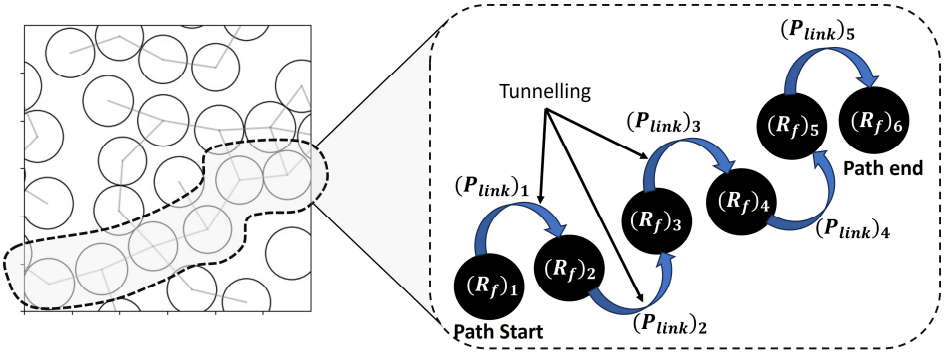

Figure 9. Quantum tunneling schematic including tunneling probabilities $(P_{link})_n$ and resistance across the n^{th} fiber cross-section $\left(R_{ft}\right)_n$ for the shortest conductive path.

2.2. Electrical Conductivity of BP

The electrical conductivity of BP at the macroscopic level is generally considered transversely isotropic, primarily because CNTs within BP are randomly oriented and lack

any inherent directional bias. Additionally, in this research, the BP conductivity is assumed to be independent of frequency. While this simplification is not entirely precise, it is reasonable for two main reasons. First, the CNTs in BP are short (~10 μm) and nonmagnetic and thus possess negligible inductance, and second, they are separated by only a few nanometers (~10 nm), as illustrated in Figure 1. At this length scale, the probability of quantum tunneling between nanotubes is notably high, facilitating the movement of electrons along many suitable conductive paths. In the through-thickness direction, due to the presence of a relatively thick matrix region, the electrical conductivity is considered similar to that of the DC transverse conductivity of the carbon fiber ply. The BP DC conductivity values used for this study are outlined in Table 1.

2.3. EMI Shielding Model

The longitudinal and transverse conductivity estimated from the equivalent circuit models explained above is used to predict the EMI SE of hybrid BP/CFRP laminates. The EMI shielding in materials is a consequence of three fundamental phenomena: reflection, absorption, and internal reflections. In the case of composites, the absorption-based shielding effect exceeds 10 dB; hence, the effect of shielding through multiple reflections is safely ignored. The EMI SE of the samples was determined using an ANSYS high-frequency structure simulator (HFSS), which uses a full-wave electromagnetic simulation technique to calculate the scattering parameters (S-parameters). The software employs the finite element boundary integral method (FEBIM) to solve Maxwell's equations that govern electromagnetic fields within each mesh element and account for interaction with exterior regions. Although the constituent properties employed for the EMI simulations are obtained from the micro-scale model explained in Section 2.1, the electromagnetic simulations themselves are conducted at the lamina scale and do not address the effects of multiple scattering at the constituent scale. For this reason, experimental testing using an appropriate setup and vector network analyzer is required to validate the ANSYS simulations.

In the modeling of each lamina, the material properties, including conductivity, permittivity, and permeability, are provided as inputs. The electrical conductivity for a lamina oriented at an arbitrary angle θ is represented in tensor form, as depicted in Equation (22) [24]. σ_L and σ_T denote the longitudinal and transverse conductivities. Due to the transversely isotropic nature of the lamina, the through-ply conductivity is assumed to be the same as the transverse conductivity. A semi-infinite representative shield element was simulated, and the scattering parameters (S-parameters) S_{11} and S_{21} were obtained for each sample under study, which allow for calculating the amplitude of the reflected and transmitted wave. A pictorial representation of a 10 mm × 10 mm rectangular waveguide used for the analysis is shown in Figure 10. To prevent boundary reflections/radiations and ensure precise results, periodic boundary conditions were applied along the walls, and Floquet ports [24] were employed at both the Inlet and Exit ports. The fundamental transverse electric mode of propagation TE_{10} was considered for the analysis due to the simplicity of the geometry and nonmagnetic nature of the specimen. This approach allowed for a comprehensive analysis of the electromagnetic response of the representative shield element under investigation.

$$\sigma_\theta = \begin{bmatrix} \sigma_L cos^2(\theta) + \sigma_T sin^2(\theta) & \frac{\sigma_L - \sigma_T}{2} sin(2\theta) & 0 \\ \frac{\sigma_L - \sigma_T}{2} sin(2\theta) & \sigma_L sin^2(\theta) + \sigma_T cos^2(\theta) & 0 \\ 0 & 0 & \sigma_T \end{bmatrix} \quad (22)$$

Using S-parameters obtained from the simulations, the shielding effectiveness due to reflection SE_R and absorption SE_A were calculated using the following relations:

$$SE_R = 10 log_{10}\left(\frac{1}{1-|S_{11}^2|}\right) \text{ [dB]} \quad (23)$$

$$SE_A = 10log_{10}\left(\frac{1-|S_{11}^2|}{|S_{21}^2|}\right) \text{ [dB]} \quad (24)$$

Finally, the total shielding effectiveness SE can be expressed as follows:

$$SE = SE_A + SE_R \quad (25)$$

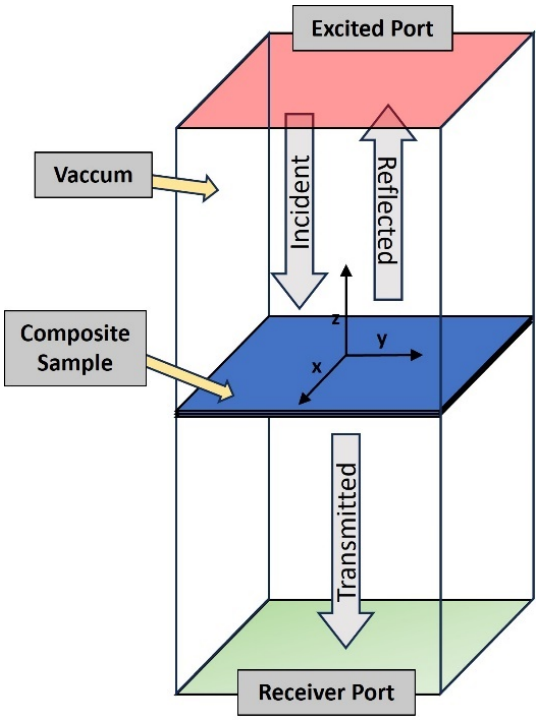

Figure 10. Waveguide model schematic showing the composite sample under study.

3. Results and Discussion

3.1. Longitudinal Electrical Conductivity

The CFRP plies exhibit high electrical conductivity in the longitudinal direction due to the long and continuous nature of fibers. Using the procedure detailed in Section 2.1, the frequency-dependent longitudinal conductivity (σ_L) of a unidirectional CFRP lamina in the 60 Hz to 50 GHz frequency range was calculated. The results are compared with experimental results obtained by Kim et al. [35] and are shown in Figure 11a. At frequencies above 0.5 GHz, the inductive reactance becomes notably pronounced, resulting in an overall reduction in conductivity. A slight variation in the location of the point where conductivity begins to reduce is observed with changes in ply size, as depicted in Figure 11b. Lamina with more fibers exhibit an earlier onset of the declining trend, while those with lesser fibers experience this decline at a later stage. This behavior can be attributed to the inverse relationship between the overall inductance of a ply in the longitudinal direction and the number of fibers within the ply, coupled with a direct proportionality to the ply length. Figure 12 depicts the overall inductance $\left(L_f\right)_{net}$ as a function of total number of fibers N, for a 1 cm long ply.

The decrease in overall inductance is a consequence of two primary factors. First, the effective inductance significantly reduces when more fibers are connected in parallel. Second, with an increasing number of fibers, the influence of mutual induction becomes negligible due to the cancelation of magnetic fields. Beyond ~5000 fibers, the net inductance saturates, which is attributed to the limited influence of distant fibers on the inductance of a given fiber.

For the case of a 10 mm × 10 mm × 0.25 mm ply with a 60% fiber volume fraction, comprising roughly 70,000 fibers, an overall inductance of ~2.5 pH was obtained. This value translated to an average fiber inductance of ~17.5 µH, which falls within the range published by other researchers [36]. Subsequently, employing this result, the frequency-dependent longitudinal conductivity σ_L can be calculated. The response obtained is cross-referenced with values documented in existing literature to validate the model [35,37]. Kim et al. [35] conducted experiments to investigate the AC conductivity of USN-150R prepregs with fiber conductivity between 600–660 S/cm. Their findings confirm the accuracy and technique of the model proposed in this study, as depicted in Figure 11a.

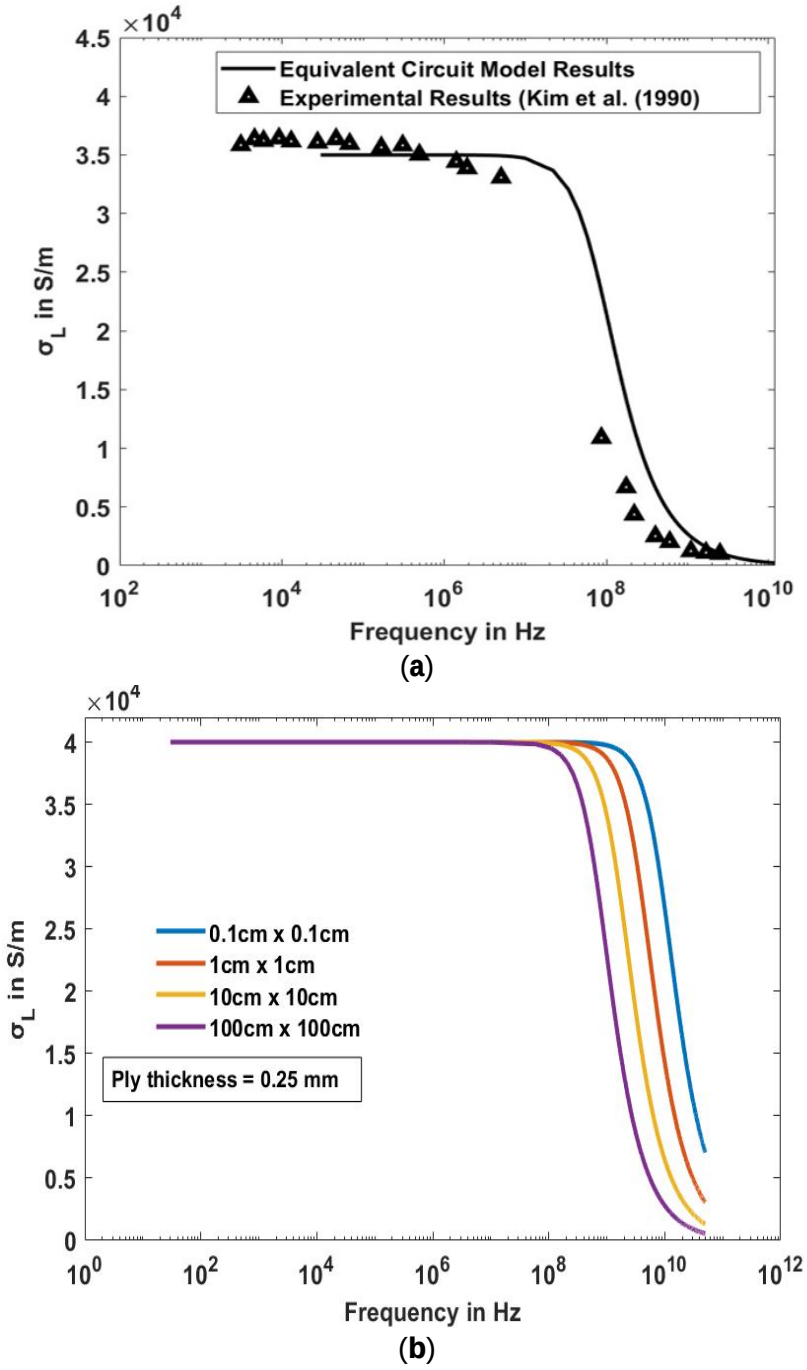

Figure 11. (**a**) Longitudinal CFRP conductivity declining at higher frequencies due to the rise of inductive reactance and (**b**) shift in conductivity decline point for different square ply sizes showing an early decline in conductivity in larger plies.

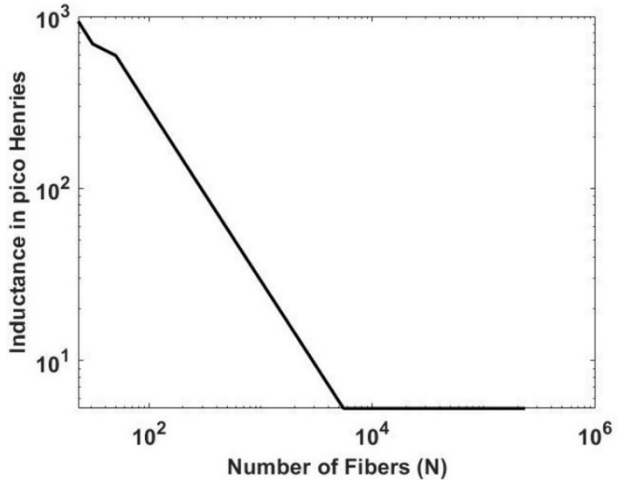

Figure 12. Overall inductance versus number of fibers on a log–log scale showing the saturation of the induction.

3.2. Transverse Electrical Conductivity

For fibers separated by a distance of less than 50 nm, the barrier potential energy is relatively low, resulting in a significant tunneling probability. Figure 13 depicts the trend of tunneling probability with signal frequency for various barrier sizes. It is observed that the tunneling probability rises with an increase in signal frequency. This holds true for all barrier sizes, as the particle's energy elevates with frequency according to Equation (17). As the barrier size diminishes, the charge can be conducted even at lower frequencies due to the reduced barrier potential energy required for passage. This observation underscores the closely packed fibers forming efficient conductive pathways along the transverse direction, leading to high electrical conductivity.

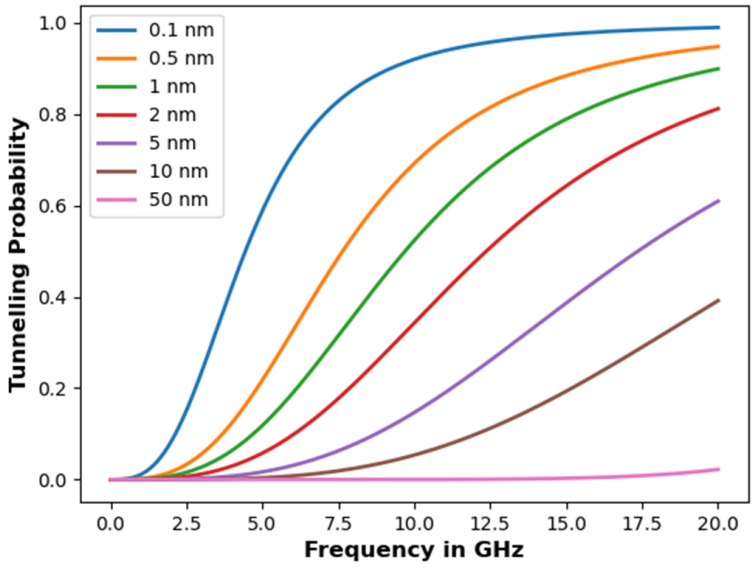

Figure 13. Tunneling probability versus signal frequency for different barrier sizes.

Another important parameter that dictates the transverse conductivity arises due to fiber waviness. The term l_c, as explained in Figure 8, is crucial in estimating the transverse conductivity of a lamina. In laminas with increased waviness, fibers tend to have multiple contacts with adjacent fibers along the longitudinal direction, thereby enhancing the probability of tunneling. The outcomes illustrated in Figure 13 correspond to a 20% fiber contact length along the fiber direction employed for this study. To understand the effect of fiber

contact length l_c, three varying degrees of fiber contact along the longitudinal direction were considered, and the results are plotted as shown in Figure 14.

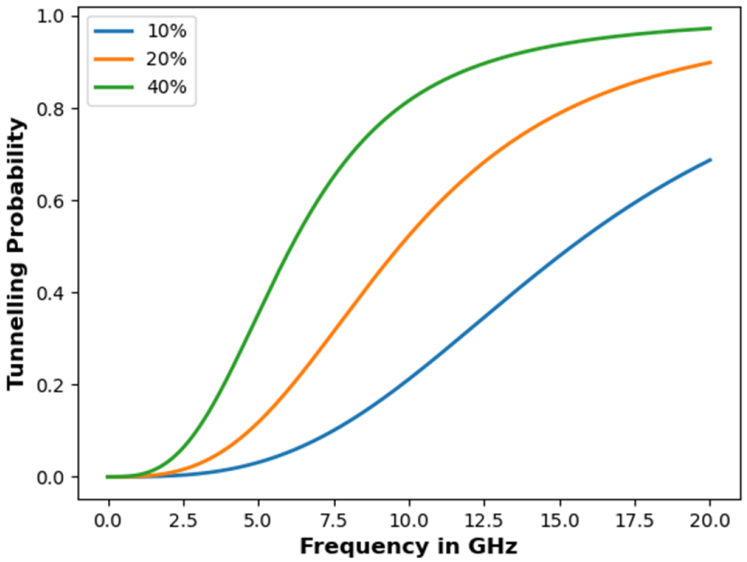

Figure 14. Tunneling probability versus signal frequency for different fiber contact lengths (contact length shown as a percentage of the entire fiber length).

The quantum tunneling-based Monte Carlo model described in Section 2.1.2 is used to generate 1000 datasets for the transverse conductivity (σ_T) in the frequency range 100 MHz to 1 GHz. Utilizing the mean and standard deviation from the dataset, σ_T was plotted with a 95% confidence interval, as shown in Figure 15. A consistent finding across all datasets is the negligible conductivity up until ~400 MHz. Beyond 450 MHz, an average transverse conductive of ~12.67 S/m and standard deviation ~1 S/m was observed, aligning with the broad spectrum of experimentally measured and simulated transverse conductivities as documented in existing literature. At frequencies above ~10 GHz, as the longitudinal conductivity rapidly declines, the transverse conductivity becomes comparatively significant and plays a crucial factor in dictating the EMI SE of CFRP composites.

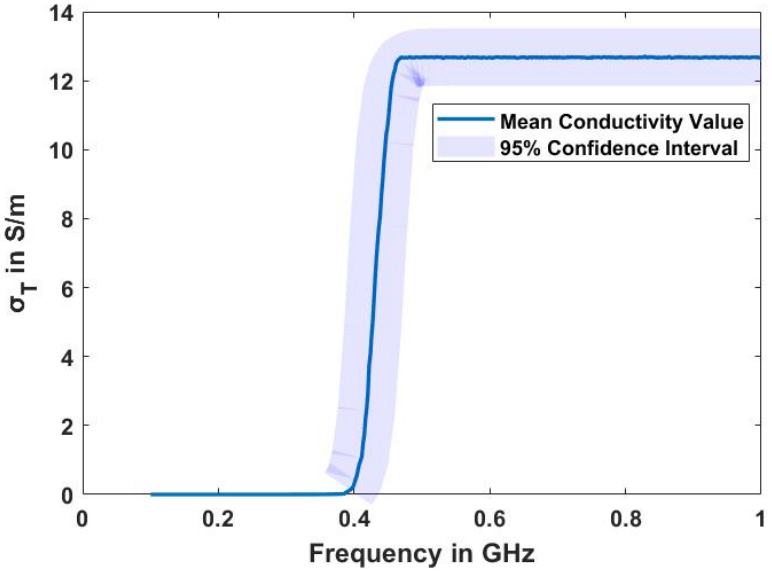

Figure 15. Transverse conductivity with a 95% confidence interval obtained from the quantum tunneling-based Monte Carlo simulations.

3.3. EMI Shielding of BP/CFRP Hybrid Composites

This study examines the effect of BP placement and relative CFRP ply orientation to understand the EMI SE of hybrid composites. All the specimen configurations used for the study are detailed in Table 4. Initially, the BP position is varied within a simple [90,0] baseline configuration to understand the effect of BP placement. Subsequently, to assess the influence of adjacent ply orientation, BP is introduced between two plies and one of the ply orientations is modified. Finally, the effects of BP in a composite with a [90, 0, ±45, 0, 90]$_s$ stacking sequence are investigated.

Table 4. Specimen configuration.

Label	Configuration
Case 1 (BP Placement)	[90, 0] [BP, 90, 0] [90, BP, 0] [90, 0, BP]
Case 2 (Adjacent Ply)	[0, BP, 0] [45, BP, 0] [90, BP, 0]
Case 3 (Standard Configuration)	[90, 0, ± 45, 0, 90]$_s$ [90, 0, BP, ± 45, 0, 90]$_s$

The total SE, along with its reflection and absorption components for a single BP film and a [90,0] baseline laminate, are shown in Figures 16a and 16b, respectively. These results show good agreement with the available literature [38–40]. At 2 GHz, the total shielding effectiveness (SE) for the BP is predicted to be approximately 43 dB, which aligns with the manufacturer's reported value of 40 dB [32]. Additionally, the total EMI SE for a [90,0] laminate with a thickness of 0.5 mm in the X-band (8 GHz to 12 GHz) is predicted to range from 62 dB to 57 dB, which is consistent with the experimental data reported in the literature. A dominant absorption effect was observed in the shielding effectiveness of the [90,0] laminate when contrasted with the BP film, owing to its thickness. It was observed that the presence of BP significantly enhances the overall SE of a composite. Particularly at frequencies exceeding 1 GHz, wherein the electrical conductivity of CFRP experiences a significant decline, the corresponding EMI SE also drops. The incorporation of BP interleaf proves effective in sustaining elevated electrical conductivity, even at higher frequencies, thereby preventing a reduction in the overall shielding effectiveness. The effect of BP location within the baseline [90,0] laminate is depicted in Figure 16c–e. By varying the position of BP within the composite, the SE also varies slightly. It was inferred that due to the complex reflection and absorption shielding mechanisms, the stacking sequence of the hybrid BP/CFRP composites greatly influences the overall shielding effectiveness.

Figure 17 illustrates the effect of ply orientations adjacent to the BP on its EMI SE. Optimal shielding against undesired radiation is attained by integrating two unidirectional plies with the greatest variation in orientation angles. The inclusion of more uniformly oriented plies aids in transitioning towards a quasi-isotropic laminate, resulting in a notable decrease in the anisotropy of electrical conductivity and enhancing the overall SE. Moreover, the isotropic nature of BP further enhances the EMI shielding performance by reducing the anisotropy in electrical properties. In the case of thicker balanced symmetric laminates, as the frequency increases, the effect of BP is more pronounced due to the drop in the CFRP conductivity. The use of BP interleaves can help significantly improve the EMI SE of thick CFRP laminates. This behavior can be observed in Figure 18, which shows the EMI SE of a 12-ply sample with and without the BP.

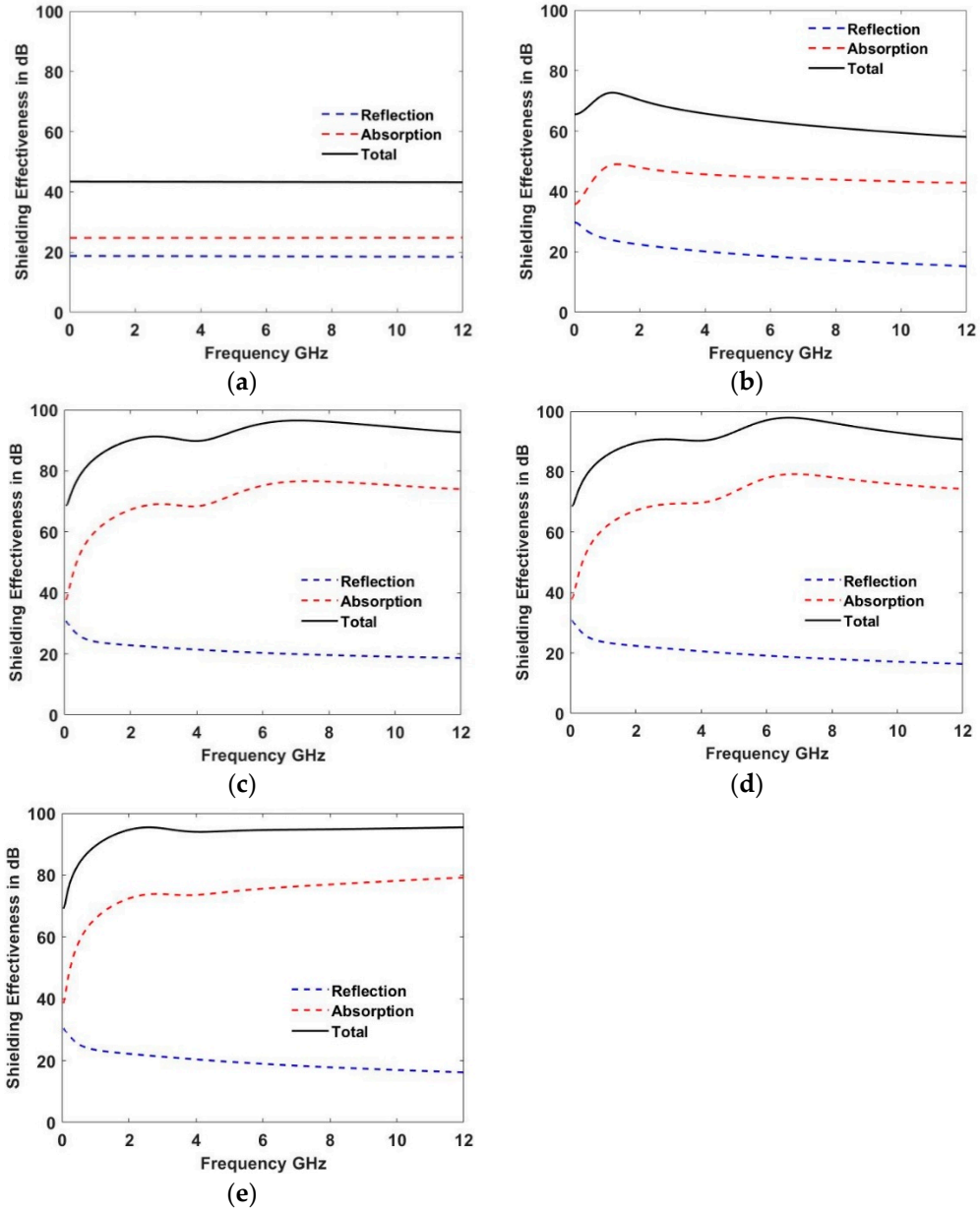

Figure 16. Shielding effectiveness in the 50 MHz–12 GHz frequency range for (**a**) buckypaper (BP), (**b**) [90,0], (**c**) [BP,90,0], (**d**) [90,BP,0], and (**e**) [90,0,BP].

Finally, the shielding effectiveness of BP is compared to other techniques, such as incorporating copper mesh [24]. Figure 19 illustrates that the EMI shielding effectiveness of BP composites remains significantly high beyond 1 GHz. This is credited to the increased electrical conductivity of the BP layer at high frequencies, in contrast to copper, which experiences a gradual decline in conductivity with frequency due to the skin effect. At elevated frequencies, instead of flowing uniformly, the current tends to concentrate on the surface of copper, thereby restricting the penetration of electromagnetic waves. The current density decreases exponentially as the wave penetrates the material, and the depth at which it falls to approximately 37% of its surface value is known as the skin depth. The skin depth decreases with increasing frequency. As a result, the effective area available for current flow is reduced, leading to a decrease in EMI SE. Additionally, BP offers a crucial advantage over metallic layers by seamlessly bonding with carbon fiber lamina without compromising mechanical performance, thereby rendering it suitable for high performance in various aspects [17].

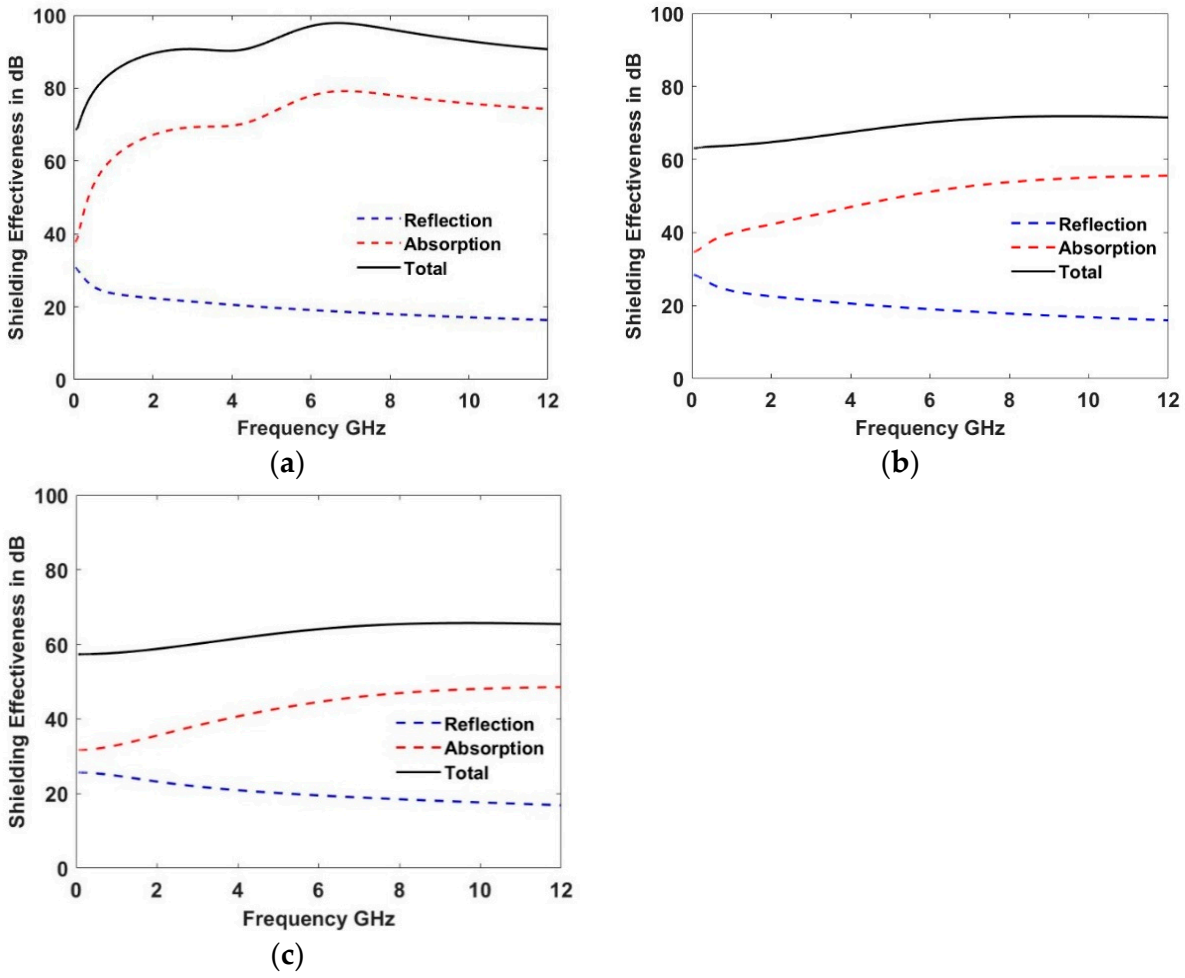

Figure 17. Effect of ply orientation on the shielding effectiveness: (**a**) [90,BP,0], (**b**) [45,BP,0], and (**c**) [0,BP,0].

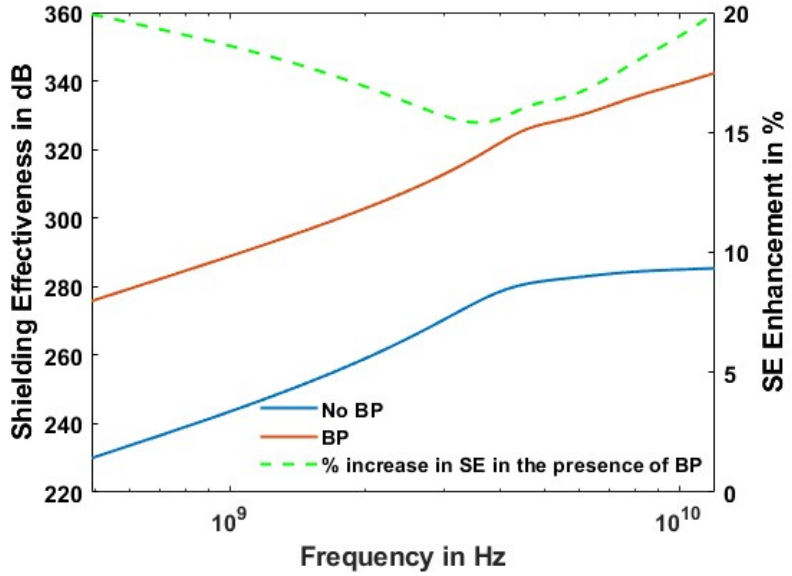

Figure 18. Effect of buckypaper (BP) on the shielding effectiveness of a 12-ply laminate showing the percentage enhancement in SE by incorporating BP.

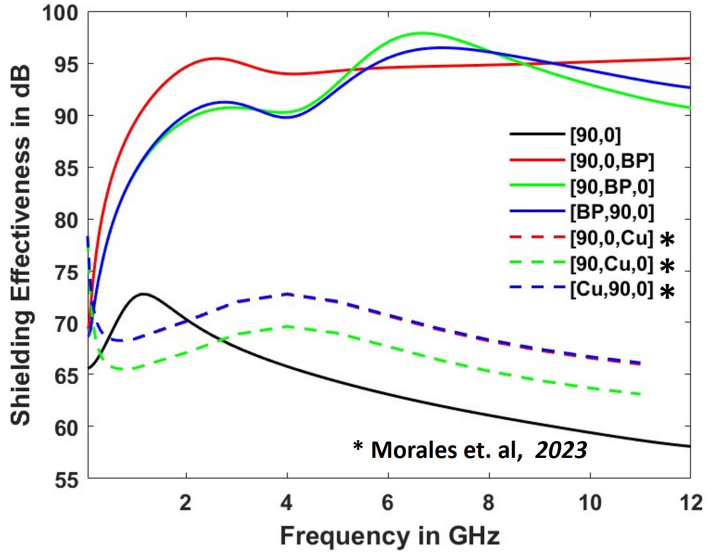

Figure 19. Comparison between the shielding effectiveness exhibited by composites with buckypaper (BP) and copper mesh interleaves [24].

4. Conclusions

This study investigates the electromagnetic interference shielding properties of hybrid buckypaper/carbon fiber-reinforced composites. A novel quantum tunneling-based equivalent circuit approach combined with Monte Carlo simulations was introduced to predict the frequency-dependent electrical conductivity of unidirectional carbon fiber lamina. The model provides an accurate approach for estimating both longitudinal and transverse electrical conductivity of unidirectional plies of arbitrary size, morphology, and constituent electrical properties. Subsequently, effective electrical properties were employed to evaluate the shielding performance of buckypaper against external electromagnetic radiation in the 50 MHz–12 GHz frequency range. The findings demonstrate a significant improvement in the overall shielding effectiveness of carbon fiber-reinforced polymer composites with the inclusion of buckypaper interleaves at high frequencies. This enhancement is attributed to the consistent electrical conductivity of buckypaper, even as the conductivity of carbon fiber lamina declines beyond 1 GHz. The integration of buckypaper into fiber-reinforced composites leads to a comprehensive improvement in both the electrical and mechanical properties, making them an ideal choice for use in composite structures.

Author Contributions: Conceptualization, A.C., T.C.H., A.H. and M.A.M.; methodology, K.T.; software, K.T.; validation, K.T.; formal analysis, K.T. and M.H.H.; investigation, K.T.; resources, A.C.; data curation, K.T.; writing—original draft preparation, K.T.; writing—review and editing, A.C. and M.H.H.; visualization, K.T.; supervision, A.C.; project administration, T.C.H., A.H. and M.A.M.; funding acquisition, A.C. All authors have read and agreed to the published version of the manuscript.

Funding: This research was funded by Army Research Laboratory grant number W911NF-17-2-0207.

Institutional Review Board Statement: Not applicable.

Informed Consent Statement: Not applicable.

Data Availability Statement: The raw data required to reproduce these findings will be made available upon request.

Acknowledgments: This research was sponsored by the Army Research Laboratory (Cooperative Agreement W911NF-17-2-0207). The views and conclusions contained in this document are those of the authors and should not be interpreted as representing the official policies, either expressed or implied, of the Army Research Laboratory or the U.S. Government. The U.S. Government is authorized to reproduce and distribute reprints for Government purposes, notwithstanding any

copyright notation herein. This article is a revised and expanded version of a paper entitled "Electrical Characterization and Electromagnetic Interference Shielding Properties of Hybrid Buckypaper-Reinforced Polymer Matrix Composites" [41], which was presented at the Aerospace Structures, Structural Dynamics, and Materials Conference at Renton, Washington on 29 April 2024.

Conflicts of Interest: The authors declare no conflicts of interest.

Nomenclature

ρ_f	Fiber resistivity
ρ_m	Matrix resistivity
ε_o	Vacuum permittivity
ε_r	Relative permittivity of medium
μ_o	Vacuum permeability
μ_r	Relative permeability of medium
n_m	Refractive Index of matrix
R_f	Fiber resistance
len_f	Fiber length
r_f	Mean fiber radius
X_L	Fiber inductive reactance
L_f	Fiber inductance
f	Signal frequency
T_{avg}	Average fiber separation
$\left\|Z_{long.}\right\|$	Longitudinal CFRP impedance
N	Number of fibers
σ_{11}	Longitudinal AC conductivity
$\hbar$	Reduced Planck's constant
m_e	Electron mass
U_o	Barrier potential energy
E	Particle's energy
a	Barrier size
C_T	Tunneling coefficient
$\|Z_c\|$	Contact impedance
R_c	Contact resistance
C_c	Contact capacitance
T	Separation between neighboring fibers
X_C	Contact capacitive reactance
l_c	Total fiber contact length
S	RVE length transverse to the fiber
l_z	RVE length along the fiber
c	Speed of light
q_e	Electron charge
σ_{22}	Transverse AC conductivity
SE_A	Absorption shielding effectiveness
SE_R	Reflection shielding effectiveness
SE	Total shielding effectiveness

Appendix A

The general solutions for wave functions Ψ_A, Ψ_B, and Ψ_C obtained from Equation (8) are given below:

$$\Psi_A(x) = C_1 e^{ik_o x} + C_2 e^{-ik_o x} \tag{A1}$$

$$\Psi_B(x) = C_3 e^{k_b x} + C_4 e^{-k_b x} \tag{A2}$$

$$\Psi_C(x) = C_5 e^{ik_o x} + C_6 e^{-ik_o x} \tag{A3}$$

where C_1, C_2, C_3, C_4, C_5, and C_6 are solution coefficients. Constants k_o and k_b can be further expressed as follows:

$$k_o = \frac{\sqrt{2m_e E}}{\hbar} \tag{A4}$$

$$k_b = \frac{\sqrt{2m_e(U-E)}}{\hbar} \tag{A5}$$

In the present case, the second term in $\Psi_C(x)$ (Equation (A3)) can be ignored because there is no interface to induce reflection; the particle is moving unidirectionally to the right. Additionally, the solution coefficient C_1 associated with the probability density of particle incident on the barrier is one. In the matrix region, denoted by B, the wave function exhibits a decaying behavior, as represented in Figure A1. Upon enforcing C^1 continuity at the two fiber matrix interfaces (x = 0 and x = a where 'a' represents the barrier size), a deterministic system of equations involving four unknowns is obtained.

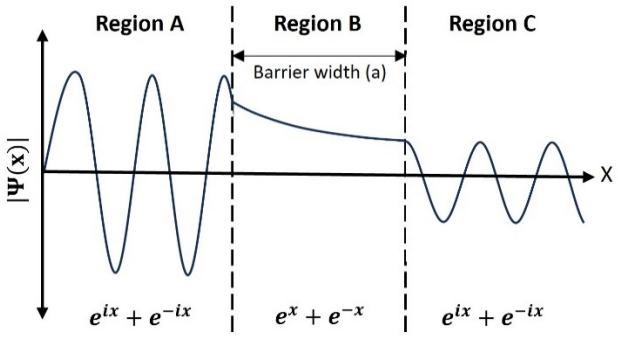

Figure A1. The wave function in the three different regions.

At the incident interface (x = 0):

$$1 + C_2 = C_3 + C_4 \tag{A6}$$

$$ik_o(1 - C_2) = k_b(C_3 - C_4) \tag{A7}$$

At the transmitted interface (x = a):

$$C_3 e^{k_b a} + C_4 e^{-k_b a} = C_5 e^{ik_o a} \tag{A8}$$

$$k_b\left(C_3 e^{k_b a} - C_4 e^{-k_b a}\right) = ik_o C_5 e^{ik_o a} \tag{A9}$$

Solving Equations (A6)–(A9), the coefficient C_5, which is linked to the tunneling probability, can be obtained. Subsequently, the transmission coefficient C_T is computed using the following equation:

$$C_T = \frac{P_t}{P_i} \tag{A10}$$

where P_t and P_i are the probability density of finding the particle as it exits the barrier in region C and the particle incident on the barrier in region A, respectively. P_t can be further expressed as a product of the wave function Ψ_C and its complex conjugate Ψ_C^* using the following expression:

$$P_t = \Psi_C \, \Psi_C^* \tag{A11}$$

Upon further simplification, P_t is found equivalent to C_5^2. Given that C_1 equals one, P_i also equals one, resulting in a streamlined tunneling probability formulation and yielding the ultimate tunneling coefficient as shown below:

$$C_T = \left(1 + \frac{\sinh^2(k_b a)}{4\eta(1-\eta)}\right)^{-1} \tag{A12}$$

where η represents the ratio of the particle's energy (E) to the barrier potential energy (U).

References

1. Iijima, S. Helical microtubules of graphitic carbon. *Nature* **1991**, *354*, 56–58. [CrossRef]
2. Eatemadi, A.; Daraee, H.; Karimkhanloo, H.; Kouhi, M.; Zarghami, N.; Akbarzadeh, A.; Abasi, M.; Hanifehpour, Y.; Joo, S.W. Carbon nanotubes: Properties, synthesis, purification, and medical applications. *Nanoscale Res. Lett.* **2014**, *9*, 393. [CrossRef] [PubMed]
3. Li, J.; Zhang, Z.; Fu, J.; Liang, Z.; Ramakrishnan, K.R. Mechanical properties and structural health monitoring performance of carbon nanotube modified FRP composites: A review. *Nanotechnol. Rev.* **2021**, *10*, 1438–1468. [CrossRef]
4. Yokozeki, T.; Iwahori, Y.; Ishiwata, S. Matrix cracking behaviors in carbon fiber/epoxy laminates filled with cup-stacked carbon nanotubes (CSCNTs). *Compos. Part A Appl. Sci. Manuf.* **2007**, *38*, 917–924. [CrossRef]
5. Du, F.; Scogna, R.C.; Zhou, W.; Brand, S.; Fischer, J.E.; Winey, K.I. Nanotube Networks in Polymer Nanocomposites: Rheology and Electrical Conductivity. *Macromolecules* **2004**, *37*, 9048–9055. [CrossRef]
6. El Sawi, I.; Olivier, P.A.; Demont, P.; Bougherara, H. Processing and electrical characterization of a unidirectional CFRP composite filled with double walled carbon nanotubes. *Compos. Sci. Technol.* **2012**, *73*, 19–26. [CrossRef]
7. Xia, X.; Wang, Y.; Zhong, Z.; Weng, G.J. A frequency-dependent theory of electrical conductivity and dielectric permittivity for graphene-polymer nanocomposites. *Carbon* **2017**, *111*, 221–230. [CrossRef]
8. Mohan, L.; Kumar, P.N.; Karakkad, S.; Krishnan, S.T. Determination of electrical percolation threshold of carbon nanotube-based epoxy nanocomposites and its experimental validation. *IET Sci. Meas. Technol.* **2019**, *13*, 1299–1304. [CrossRef]
9. Guadagno, L.; Vertuccio, L.; Naddeo, C.; Raimondo, M.; Barra, G.; De Nicola, F.; Volponi, R.; Lamberti, P.; Spinelli, G.; Tucci, V. Electrical Current Map and Bulk Conductivity of Carbon Fiber-Reinforced Nanocomposites. *Polymers* **2019**, *11*, 1865. [CrossRef] [PubMed] [PubMed Central]
10. Ma, P.-C.; Siddiqui, N.A.; Marom, G.; Kim, J.-K. Dispersion and functionalization of carbon nanotubes for polymer-based nanocomposites: A review. *Compos. Part A Appl. Sci. Manuf.* **2010**, *41*, 1345–1367. [CrossRef]
11. Zhao, Q.; Zhang, K.; Zhu, S.; Xu, H.; Cao, D.; Zhao, L.; Zhang, R.; Yin, W. Review on the Electrical Resistance/Conductivity of Carbon Fiber Reinforced Polymer. *Appl. Sci.* **2019**, *9*, 2390. [CrossRef]
12. Gojny, F.H.; Wichmann, M.H.G.; Fielder, B.; Bauhofer, W.; Schulte, K. Influence of nano-modification on the mechanical and electrical properties of conventional fibre-reinforced composites. *Compos. Part A Appl. Sci. Manuf.* **2005**, *36*, 1525–1535. [CrossRef]
13. Schulz, S.C.; Schlutter, J.; Bauhofer, W. Influence of Initial High Shearing on Electrical and Rheological Properties and Formation of Percolating Agglomerates for MWCNT/Epoxy Suspensions. *Macromol. Mater. Eng.* **2010**, *295*, 613–617. [CrossRef]
14. Song, Y.S.; Youn, J.R. Influence of dispersion states of carbon nanotubes on physical properties of epoxy nanocomposites. *Carbon* **2005**, *43*, 1378–1385. [CrossRef]
15. Datta, S.; Fard, M.Y.; Chattopadhyay, A. High-Speed Surfactant-Free Fabrication of Large Carbon Nanotube Membranes for Multifunctional Composites. *J. Aerosp. Eng.* **2015**, *29*, 04015060. [CrossRef]
16. Li, Z.; Liang, Z. Optimization of Buckypaper-enhanced Multifunctional Thermoplastic Composites. *Sci. Rep.* **2017**, *7*, 42. [CrossRef]
17. Tripathi, K.; Hamza, M.H.; Chattopadhyay, A.; Henry, T.C.; Hall, A. Impact of buckypaper on the mechanical properties and failure modes of composites. In Proceedings of the American Society for Composites-Thirty-Eighth Technical Conference, Woburn, MA, USA, 18–20 September 2023.
18. Munalli, D.; Dimitrakis, G.; Chronopoulos, D.; Greedy, S.; Long, A. Electromagnetic shielding effectiveness of carbon fibre reinforced composites. *Compos. Part B Eng.* **2019**, *173*, 106906. [CrossRef]
19. Banerjee, P.; Schmidt, J.L. Electrical conductivity modeling and validation in unidirectional carbon fiber reinforced polymer composites. In Proceedings of the COMSOL Conference, Rotterdam, The Netherlands, 23–25 October 2013.
20. Wasselynck, G.; Trichet, D.; Fouladgar, J. Determination of the Electrical Conductivity Tensor of a CFRP Composite Using a 3-D Percolation Model. *IEEE Trans. Magn.* **2013**, *49*, 1825–1828. [CrossRef]
21. Wasselynck, G.; Trichet, D.; Ramdane, B.; Fouladgar, J. Microscopic and Macroscopic Electromagnetic and Thermal Modeling of Carbon Fiber Reinforced Polymer Composites. *IEEE Trans. Magn.* **2011**, *47*, 1114–1117. [CrossRef]
22. Hirano, Y.; Yamane, T.; Todoroki, A. Through-thickness electric conductivity of toughened carbon-fibre-reinforced polymer laminates with resin-rich layers. *Compos. Sci. Technol.* **2016**, *122*, 67–72. [CrossRef]
23. Zhang, R.; Bin, Y.; Chen, R.; Matsuo, M. Evaluation by tunneling effect for the temperature-dependent electric conductivity of polymer-carbon fiber composites with visco-elastic properties. *Polym. J.* **2013**, *45*, 1120–1134. [CrossRef]
24. Morales, M.A.; Henry, T.C.; Salamanca-Riba, L.G. Model of electromagnetic interference shielding effectiveness for a multifunctional composite containing carbon-fiber-reinforced polymer and copper mesh layers. *Carbon* **2023**, *212*, 118179. [CrossRef]
25. Mostafavi Yazdi, S.J.; Lisitski, A.; Pack, S.; Hiziroglu, H.R.; Baqersad, J. Analysis of Shielding Effectiveness against Electromagnetic Interference (EMI) for Metal-Coated Polymeric Materials. *Polymers* **2023**, *15*, 1911. [CrossRef] [PubMed]
26. Hu, S.; Wang, D.; Kyosev, Y.; Kremenakova, D.; Militky, J. The novel approach of EMI shielding simulation for metal coated nonwoven textiles with optimized textile module. *Polym. Test.* **2022**, *114*, 107706. [CrossRef]
27. Liu, Y.; Song, D.; Wu, C.; Leng, J. EMI shielding performance of nanocomposites with MWCNTs, nanosized Fe_3O_4 and Fe. *Compos. Part B Eng.* **2014**, *63*, 34–40. [CrossRef]

28. Karimi, P.; Ostoja-Starzewski, M.; Jasiuk, I. Experimental and computational study of shielding effectiveness of polycarbonate carbon nanocomposites. *J. Appl. Phys.* **2016**, *120*, 145103. [CrossRef]
29. Zhang, M.; Cao, M.-S. Assembly of Multi-Dimensional Microstructures of MXene towards Wearable Electromagnetic Attenuating Devices. *Crystals* **2023**, *13*, 1612. [CrossRef]
30. Holloway, C.L.; Sarto, M.S.; Johansson, M. Analyzing carbon-fiber composite materials with equivalent-Layer models. *IEEE Trans. Electromagn. Compat.* **2005**, *47*, 833–844. [CrossRef]
31. Available online: https://3937524.app.netsuite.com/core/media/media.nl?id=172313&c=3937524&h=dab869f57f81854c6a97&_xt=.pdf (accessed on 8 September 2024).
32. Available online: https://www.huntsman.com/docs/Documents/MIRALON%20Sheet%20Technical%20Datasheet.pdf (accessed on 8 September 2024).
33. Matsuo, S.; Sottos, N.R. Single carbon fiber transverse electrical resistivity measurement via the van der Pauw method. *J. Appl. Phys.* **2021**, *130*, 115105. [CrossRef]
34. Maradei, F.; Caniggia, S. Appendix A: Formulae for partial inductance calculation. In *Signal Integrity and Radiated Emission of High-Speed Digital Systems*; Francescaromana, M., Caniggia, S., Eds.; John Wiley & Sons, Ltd.: Hoboken, NJ, USA, 2008; pp. 481–486.
35. Kim, H.C.; See, S.K. Electrical properties of unidirectional carbon-epoxy composites in wide frequency band. *J. Phys. D Appl. Phys.* **1990**, *23*, 916. [CrossRef]
36. Sun, J.; Li, X.; Tian, X.; Chen, J.; Yao, X. Dynamic electrical characteristics of carbon fiber-reinforced polymer composite under low intensity lightning current impulse. *Adv. Compos. Lett.* **2020**, *29*, 2633366X20942775. [CrossRef]
37. Galehdar, A.; Rowe, W.S.T.; Ghorbani, K.; Callus, P.J.; John, S.; Wang, C.H. The Effect of Ply Orientation on the Performance of Antennas in or on Carbon Fiber Composites. *Prog. Electromagn. Res.* **2011**, *116*, 123–136. [CrossRef]
38. Rea, S.; Linton, D.; Orr, E.; McConnell, J. Electromagnetic shielding properties of carbon fibre composites in avionic systems. *Microw. Rev.* **2005**, *29*, 29–32.
39. Mikinka, E.; Siwak, M. Recent advances in electromagnetic interference shielding properties of carbon-fibre-reinforced polymer composites—A topical review. *J. Mater. Sci. Mater. Electron.* **2021**, *32*, 24585–24643. [CrossRef]
40. Guan, H.; Chung, D. Effect of the planar coil and linear arrangements of continuous carbon fiber tow on the electromagnetic interference shielding effectiveness, with comparison of carbon fibers with and without nickel coating. *Carbon* **2019**, *152*, 898–908. [CrossRef]
41. Tripathi, K.; Morales, M.; Hamza, M.H.; Henry, T.C.; Hall, A.; Chattopadhyay, A. Electrical Characterization and Electromagnetic Interference Shielding Properties of Hybrid Buckypaper Reinforced Polymer Matrix Composites. In Proceedings of the ASME 2024 Aerospace Structures, Structural Dynamics, and Materials Conference, Renton, WA, USA, 29 April–1 May 2024; ASME: New York, NY, USA, 2024; p. V001T01A006. [CrossRef]